
INVERSION OF SEA SURFACE CURRENTS FROM SATELLITE-DERIVED SST-SSH SYNERGIES WITH 4DVARNETS

A PREPRINT

Ronan Fablet

IMT Atlantique, Lab-STICC, INRIA team Odyssey
Brest, France
ronan.fablet@imt-atlantique.fr

Bertrand Chapron

Ifremer, LOPS, INRIA team Odyssey
Brest, France
bertrand.chapron@ifremer.fr

Julien Le Sommer

CNRS, IGE
Grenoble, France
julien.lesommer@univ-grenoble-alpes.fr

Florian Sévellec

CNRS, LOPS
Brest, France
florian.sevellec@univ-brest.fr

January 9, 2023

ABSTRACT

Satellite altimetry is a unique way for direct observations of sea surface dynamics. This is however limited to the surface-constrained geostrophic component of sea surface velocities. Ageostrophic dynamics are however expected to be significant for horizontal scales below 100 km and time scale below 10 days. The assimilation of ocean general circulation models likely reveals only a fraction of this ageostrophic component. Here, we explore a learning-based scheme to better exploit the synergies between the observed sea surface tracers, especially sea surface height (SSH) and sea surface temperature (SST), to better inform sea surface currents. More specifically, we develop a 4DVarNet scheme which exploits a variational data assimilation formulation with trainable observations and *a priori* terms. An Observing System Simulation Experiment (OSSE) in a region of the Gulf Stream suggests that SST-SSH synergies could reveal sea surface velocities for time scales of 2.5-3.0 days and horizontal scales of 0.5° - 0.7° , including a significant fraction of the ageostrophic dynamics ($\approx 47\%$). The analysis of the contribution of different observation data, namely nadir along-track altimetry, wide-swath SWOT altimetry and SST data, emphasizes the role of SST features for the reconstruction at horizontal spatial scales ranging from $1/20^\circ$ to $1/4^\circ$.

Keywords sea surface velocity reconstruction · satellite ocean remote sensing · satellite altimetry · deep learning · 4DVarNet · ageostrophic ocean dynamics

1 Introduction

Satellite altimeters provide the main source of observations to inform sea surface dynamics on a regional and global scale [Chelton et al., 2001]. Their scarce space-time sampling of the sea surface prevents to recover spatial scales below 100 km and time scales below 10 days in general [Ballarotta et al., 2019]. Also altimetry can only reconstruct geostrophic velocities. As stressed by simulation and observational studies, the ageostrophic components are however critical features of upper ocean dynamics regarding for instance vertical mixing properties [Mahadevan and Tandon, 2006], Lagrangian dynamics at sea surface [Baaklini et al., 2021, Sun et al., 2022].

Retrieving sea surface currents at finer scales with both their geostrophic and ageostrophic components naturally arises as a key challenge. This has motivated a large research effort both in terms of simulation studies [Uchida et al., 2022], observational effort [Villas Boas et al., 2019, Arduin et al., 2019], and data assimilation methods [Moore et al., 2019, Storto et al., 2019]. Regarding the latter aspect, state-of-the-art approaches mostly rely on the one hand on optimal interpolation approaches [Taburet et al., 2019] and on the other hand on data assimilation schemes combined with

ocean general circulation models [Baaklini et al., 2021, Benkiran et al., 2021, Fujii et al., 2019]. As mentioned above, both approaches still show limitations in the ability to retrieve fine-scale patterns, whereas both observation-driven and theoretical studies evidence the interplay between fine-scale sea surface dynamics and some observed processes such as sea surface tracers [Ciani et al., 2021, Isern-Fontanet et al., 2006] and drifters’ trajectories [Sun et al., 2022].

From a methodological point of view, data-driven and learning-based schemes have also received a growing attention to solve inverse problems in geoscience [Alvera-Azcárate et al., 2007, Lguensat et al., 2017, Barth et al., 2020]. Especially, deep learning schemes appears as appealing schemes for the reconstruction of sea surface dynamics from irregularly-sampled satellite-derived observations [Fablet et al., 2021a, 2022, George et al., 2021, Manucharyan et al., 2021]. Interestingly, these studies open new research avenues to make the most of available simulation and observation datasets. They also suggest potential breakthrough through the ability to exploit the synergies between different sea surface observational fields with no explicitly-known relationship [Fablet et al., 2022].

In this study, we exploit these recent methodological advances to explore satellite-derived SST-SSH synergies to inform sea surface currents, including their ageostrophic component. We exploit and adapt multi-modal 4DVarNet schemes introduced in [Fablet et al., 2022]. Through an observing system simulation experiment for a region of the Gulf Stream, our key contributions are four-fold:

1. We stress the potential of physics-informed deep learning schemes to enhance the reconstruction of sea surface currents (SSC) with a relative improvement greater than 50% in terms of resolved space-time scales and mean-square-error metrics compared with the state-of-the-art products;
2. Our results also support wide-swath SWOT altimetry data to improve the reconstruction of SSC fields with a potential gain of $\approx 30\%$ for most performance metrics, though the reported improvement is marginal for the divergent component of the SSC.
3. We emphasize the contribution of SST-SSH synergies to retrieve a significant fraction of the ageostrophic component of the SSC, typically $\approx 47\%$ in terms of divergence of the SSC fields, with a major contribution of SST features in the spatial scale range of $1/20^\circ$ - $1/4^\circ$.
4. We point out that, as hypothesized from theoretical considerations [Sévellec et al., 2022], the strain of sea surface dynamics partially explains ($\approx 60\%$) the time-averaged mean square error of the SSC.

We further discuss the implications of these results in the context of ongoing research efforts towards the monitoring of upper ocean dynamics.

2 Problem statement

Geostrophic and ageostrophic sea surface dynamics: The horizontal momentum equations together with the hydrostatic equilibrium for the vertical momentum and the non-divergence leads to the following set of equations to describe sea surface dynamics:

$$D_t u - f v = -\frac{1}{\rho_0} \partial_x P + \mathcal{F}_x, \quad (1a)$$

$$D_t v + f u = -\frac{1}{\rho_0} \partial_y P + \mathcal{F}_y, \quad (1b)$$

$$0 = -\frac{1}{\rho_0} \partial_z P - \frac{g}{\rho_0} \rho, \quad (1c)$$

$$\partial_x u + \partial_y v + \partial_z w = 0, \quad (1d)$$

where u , v and w are the zonal, meridional, and vertical velocities, respectively, t is time, x , y and z are the longitude, latitude, and depth, respectively, $\rho_{(0)}$ is the (reference) density for seawater, P is the pressure, f is the Coriolis parameter, g is the acceleration due to gravity, \mathcal{F}_x and \mathcal{F}_y are the action of the zonal and meridional viscous forces, respectively, and $D_t (= \partial_t + u \partial_x + v \partial_y + w \partial_z)$ is the material derivative.

These equations are often simplified to reflect the geostrophic balance which occurs under the small Rossby number ($Ro \ll 1$ i.e., inertial terms are negligible), slow dynamics ($\partial_t \rightarrow 0$ for the horizontal momentum equation), large Péclet number ($Pe \ll 1$ i.e., viscous terms are negligible), and away from direct forcing. This reads:

$$-f v_g = -\frac{1}{\rho_0} \partial_x P, \quad (2a)$$

$$+f u_g = -\frac{1}{\rho_0} \partial_y P, \quad (2b)$$

where u_g and v_g are the zonal and meridional geostrophic velocities, respectively. This formulation still implies an horizontal divergence, which, using (2) with (1d), reads:

$$\partial_x u_g + \partial_y v_g = -\frac{\beta}{f} v_g, \quad (3)$$

where $\beta (= \partial_y f)$ accounts for the meridional variation of Earth equivalent rotation rate. Hence, the horizontal momentum equations for the ageostrophic components become:

$$D_t u - f v_a = \mathcal{F}_x, \quad (4a)$$

$$D_t v + f u_a = \mathcal{F}_y, \quad (4b)$$

where u_a and v_a are the zonal and meridional ageostrophic velocities, respectively. This last set of equations show the complexity of the ageostrophic components through the action of viscous terms and of the full inertial terms in (4), compared to the rather simple linear relationships between pressure gradients and geostrophic velocities in (2). This is worth noting that boundary conditions, such as observed at the ocean surface, occurred though the actions of the viscous terms (\mathcal{F}_x and \mathcal{F}_y). This further suggests the key role of the ageostrophic terms when studying the surface velocities.

In the subsequent, for the sake of simplicity, we will refer to geostrophically-derived sea surface velocities from SSH fields from (2) using $\text{SSH} = (P|_{z=0} - P_{\text{atm}})/g\rho_s$ [where $P|_{z=0}$ is the pressure at the geoid ($z = 0$), P_{atm} is the atmospheric pressure, and ρ_s is the assumed-vertically-constant density of the surface layer] as SSH-derived sea surface currents.

Data assimilation for sea surface dynamics: Classically, inverse problems in geoscience [Evensen, 2009] are stated as data assimilation problems through some underlying state-space formulation

$$\begin{cases} \frac{\partial \mathbf{x}(t)}{\partial t} = \mathcal{M}(\mathbf{x}(t)) + \eta(t) \\ \mathbf{y}_m(t) = \mathcal{H}_m(\mathbf{x}(t)) + \epsilon_m(t), \forall t, m \end{cases} \quad (5)$$

where \mathbf{x} is the space-time process to be reconstructed and \mathbf{y}_m is an observation process which relates to state \mathbf{x} through observation operator \mathcal{H}_m for observation modality k . When dealing with irregularly-sampled observations, operator \mathcal{H}_m accounts for sampling masks. Processes η and ϵ refer to random processes to account for modeling uncertainties and observation noise, respectively. \mathcal{M} refers to the dynamical prior on state x . Given this state-space formulation, the data assimilation problem for the reconstruction of state x given observation data $\{y_k\}_k$ comes to the resolution of a minimization problem. Within a variational data assimilation framework, it generally writes as:

$$\hat{\mathbf{x}} = \arg \min_{\mathbf{x}} \sum_m \lambda_m \|\mathbf{y}_m - \mathcal{H}_m(\mathbf{x})\|^2 + \gamma \|\mathbf{x} - \Phi_{\mathcal{M}}(\mathbf{x})\|^2 \quad (6)$$

with $\{\lambda_m\}$ and γ Lagrangian multipliers, $\Phi_{\mathcal{M}}(\mathbf{x})$ the time-stepping operator to propagate one-step-ahead state \mathbf{x} at time t to time $t + \Delta t$ based on dynamical prior \mathcal{M} . In the above formulation, we consider a matrix form and drop the time variable such that the norms are evaluated as a sum over a given time interval $[0, T]$ according to time step Δt . Given dynamical prior \mathcal{M} and observation operators $\{\mathcal{H}_m\}_m$, data assimilation methods provide different algorithms [Carrassi et al., 2018, Evensen, 2009] to solve this minimization problem especially using adjoint-based gradient descent schemes and Kalman methods. Formulation (6) also relates to Optimal interpolation [Cressie and Wikle, 2015] when considering a single observation term with a masking operator operator and a prior given by a Gaussian process. Under these hypotheses, one can derive the analytical solution of the resulting linear-quadratic variational cost.

The state-of-the-art methods for the reconstruction of sea surface dynamics from satellite-derived observations rely on such data assimilation schemes. While the reconstruction of geostrophic sea surface dynamics may be stated as a space-time interpolation of satellite altimetry data [Taburet et al., 2019], the inference of the total sea surface currents from satellite-derived observations using the set of equations introduced above implies to reconstruct not only these velocities, but the whole ocean state. The assimilation of satellite altimetry and satellite-derived SST observations, possibly complemented by other data sources, in ocean general circulation models [Benkiran et al., 2021, Fujii et al., 2019] follows this strategy. An alternative approach relies on assimilation schemes with a simplified prior on sea surface dynamics, which only depend on sea surface velocities. Quasi-geostrophic (QG) dynamics are examples of such priors [Le Guillou et al., 2020, Ubelmann et al., 2014]. Similarly to the above-mentioned OI schemes, the latter only applies to geostrophic velocities and cannot recover ageostrophic components.

Recently, a rich literature has emerged to bridge data assimilation and deep learning [Abdalla et al., 2021, Barthelemy et al., 2021, Boudier et al., 2020, Bocquet et al., 2020, Fablet et al., 2021b, Nonnenmacher and Greenberg, 2021]. It provides new minimization schemes as well as new means to explore data assimilation problems when the observation operators and/or the dynamical priors are not explicitly known. As such, it opens new avenues to balance the complexity of the inversion problem and the genericity of the underlying variational formulation in (6). Here, as detailed in the subsequent, we benefit from the generic 4DVarNet framework introduced in [Fablet et al., 2021b] and explore a learning-based data assimilation schemes for the reconstruction of sea surface currents from multimodal satellite-derived observations.

3 Data

3.1 Case-study region and NATL60 data

The considered case study focuses on a $10^\circ \times 10^\circ$ region between (33°N , 65°W) and (43°N , 55°W). As illustrated in Fig. 1, this region involves the main meander of the Gulf Stream as well as a variety of mesoscale eddies and finer-scale sub-mesoscale filaments. It also comprises clear divergent features associated with the ageostrophic flow component, which makes it suitable for the current study.

The considered simulation dataset relies on a nature run of the NATL60 configuration [Ajayi et al., 2020] of the NEMO (Nucleus for European Modeling of the Ocean) model [Madec et al., 2022]. This simulation delivers a realistic hindcast simulation of ocean dynamics, including mesoscale-to-submesoscale ocean dynamics, [Ajayi et al., 2020] over one year from October 2012 to September 2013. It has been used in numerous studies regarding the reconstruction and observability of sea surface dynamics (see below for the related OSSE data challenge stated in [Le Guillou et al., 2020]).

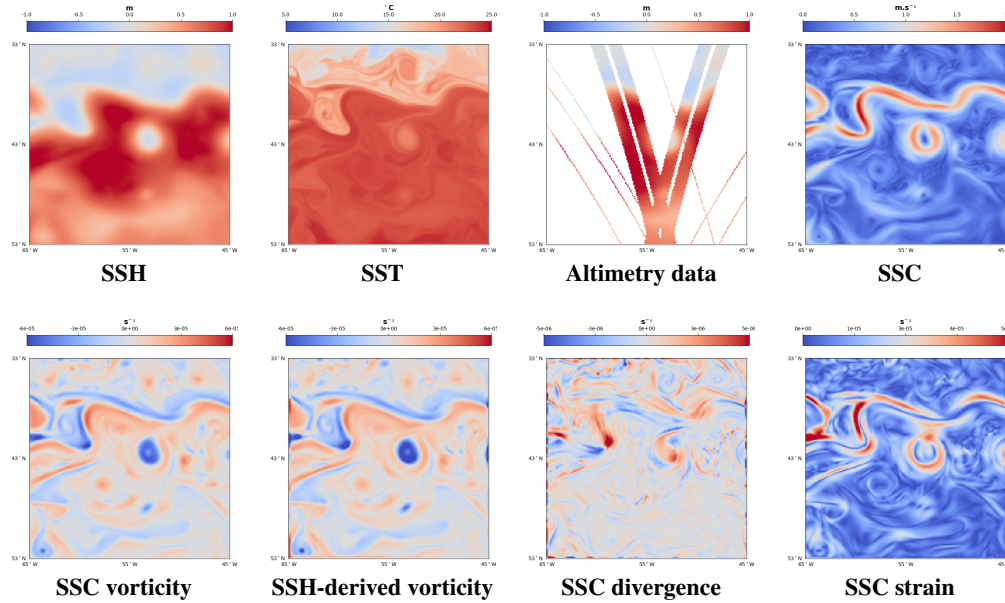


Figure 1: **Illustration of the considered case-study using NATL60 simulation dataset:** first row, from left to right, NATL60 SSH field on November 12th, associated SST field and SSH observation data from nadir and wide-swath SWOT altimeters, SSC field. The second row depicts the vorticity fields for the total currents and SSH-geostrophically-derived ones along with the divergence and strain of the total currents.

3.2 OSSE setting

Our numerical experiments exploit an Observing System Simulation Experiment (OSSE). We rely on the OSSE setting¹ proposed in [Le Guillou et al., 2020] for the benchmarking of SSH mapping methods in the context of upcoming wide-swath altimetry mission SWOT [Gaultier et al., 2015]. For a $1/20^\circ$ spatial resolution, this OSSE dataset comprises daily-averaged SSH fields and simulated altimetry data. The latter combine simulated nadir along-track data according

¹https://github.com/ocean-data-challenges/2020a_SSH_mapping_NATL60

to real 4-altimeter configuration and SWOT altimetry data using SWOT simulator [Gaultier et al., 2015]. We may point out that simulated altimetry data are created from hourly SSH fields.

In this study, we complement this initial OSSE dataset with two additional data sources with the same $1/20^\circ$ spatial resolution: the series of daily-averaged sea surface currents (SSC) and the series of daily-averaged sea surface temperature (SST). We also generate SST observations with resolutions of $1/10^\circ$, $1/5^\circ$, $1/4^\circ$ and $1/2^\circ$ using coarsening and subsampling operations to provide a more realistic simulations of the diversity of operational L4 SST products [Donlon et al., 2012, O’Carroll et al., 2019]. We report in Fig. 1 an illustration of the considered dataset.

For the training configuration, we split the one-year time series into training, validation, and test datasets according to the following time periods: from February 4th 2013 to September 30th 2013, from January 1st 2013 to February 4th 2013, and from October 20th 2012 to December 4th 2012, respectively.

4 Methods

This Section presents the proposed 4DVarNet scheme for the reconstruction of sea surface currents from satellite-derived SST-SSH synergies. We first detail the considered 4DVarNet architecture before describing our learning scheme.

4.1 Proposed 4DVarNet scheme

4DVarNet schemes refer to end-to-end neural architectures introduced in [Fablet et al., 2021b] to solve data assimilation problems and further extended to multimodal inversion schemes in [Fablet et al., 2022]. As sketched in Fig. 2, the proposed 4DVarNet scheme exploits as inputs time series of satellite altimetry data and SST fields and outputs gap-free SSH fields and SSC fields. Importantly, it combines two main components: the definition of the underlying variational formulation (7), the iterative update rule of the associated trainable gradient-based solver. The latter relies at each iteration on the gradient of the variational cost w.r.t. the state using automatic differentiation tools embedded in deep learning frameworks such as PyTorch. Overall, the 4DVarNet scheme implements a predefined number, typically from 5 to 15, of the iterative update rule to map the input partial observations to the reconstructed sea surface dynamics. We refer the reader to [Fablet et al., 2021b] for a detailed presentation of the 4DVarNet framework along with its link to variational data assimilation formulations.

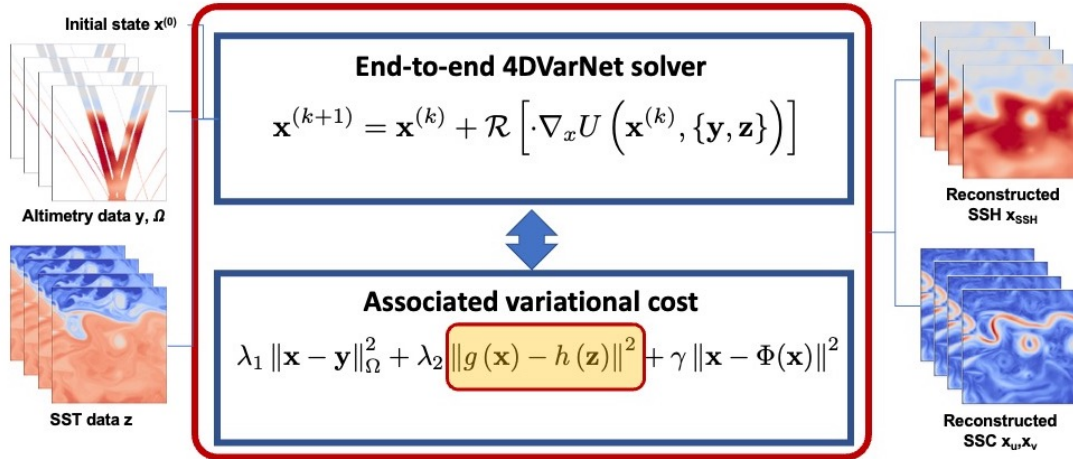


Figure 2: **Sketch of 4DVarNet scheme for the reconstruction of sea surface current fields:** 4DVarNet provides an end-to-end neural architecture to map multimodal observation data, here satellite-derived SSH and SST observations, to SSH and SSC fields. It relies on a variational data assimilation and on the resolution of the associated minimization issue with a trainable gradient-based descent. We refer the reader to [Fablet et al., 2021b] for a detailed presentation of 4DVarNet scheme.

Let us formally introduce the considered variational formulation. Let \mathbf{x} denote hereafter the space-time state to be reconstructed, \mathbf{y} the observed altimetry data and \mathbf{z} the SST observations. The considered variational cost, denoted by $U_{\Phi}(\mathbf{x}, \mathbf{y}, \mathbf{z})$, is given by:

$$U_{\Phi}(\mathbf{x}, \mathbf{y}, \mathbf{z}) = \lambda_1 \|\mathbf{x} - \mathbf{y}\|_{\Omega}^2 + \lambda_2 \|g(\mathbf{x}) - h(\mathbf{z})\|^2 + \gamma \|\mathbf{x} - \Phi(\mathbf{x})\|^2, \quad (7)$$

where λ_1 , λ_2 , and γ are Lagrangian multipliers. State \mathbf{x} combines SSH denoted by \mathbf{x}_{SSH} and the meridional and zonal SSC components denoted by \mathbf{x}_u and \mathbf{x}_v , such that

and SSC components referred to as \mathbf{x}_{SSH} and \mathbf{x}_{SSC} such that $\mathbf{x} = (\mathbf{x}_{\text{SSH}}, \mathbf{x}_u, \mathbf{x}_v)$. Besides, as in [Fablet et al., 2022], we adopt a two-scale decomposition of the SSH fields to explicitly use both raw altimetry data and DUACS coarse-scale interpolation as observation data². Ω refers to a masking operator to account for observation gaps in the altimetry data as well as for the fact that the SSC component is never directly observed.

Operators $g(\cdot)$ and $h(\cdot)$ are trainable operators which aim at extracting relevant features from SST observations z to match features extracted from state x . Following [Fablet et al., 2022], we parameterize $g(\cdot)$ and $h(\cdot)$ as non-linear convolutional networks using four convolutional layers and tanh activations. In our experiments, we exploit a 20-dimensional feature space for multimodal term $\|g(\mathbf{x}) - h(\mathbf{z})\|^2$.

Operator Φ states the considered prior onto the space-time dynamics of state \mathbf{x} . Within a classic model-driven approach, Φ would refer to the time-stepping operator to forecast future states from an initial condition. Following [Fablet et al., 2021b, 2022], we rather consider a purely data-driven parameterization with a two-scale U-Net architectures [Cicek et al., 2016]. The latter proved to be more relevant in previous numerical experiments for both Lorenz’s systems [Fablet et al., 2021b] and SSH mapping [Beauchamp et al., 2022, Fablet et al., 2022].

As sketched in Fig. 2, the considered 4DVarNet schemes implement the following iterative gradient-based solver to minimize variational cost (7):

$$\begin{cases} \mathbf{h}(k+1), \mathbf{c}(k+1) &= \mathcal{R}[\cdot \nabla_x U(\mathbf{x}^{(k)}, \{\mathbf{y}, \mathbf{z}\}), \mathbf{h}(k), \mathbf{c}(k)] \\ \mathbf{x}^{(k+1)} &= \mathbf{x}^{(k)} - \mathcal{L}(\mathbf{h}^{(k+1)}) \end{cases} \quad (8)$$

with \mathcal{R} a LSTM cell, \mathcal{L} a linear operator, $(\mathbf{h}(k), \mathbf{c}(k))$ the internal state of the LSTM cell at iteration k and $\mathbf{x}^{(k)}$ the reconstructed state at iteration k . As mentioned above, we consider 4DVarNet schemes with 5 to 15 iterations. The LSTM cell is a 2D-convolutional LSTM cell with 150-dimensional internal states. The considered iterative rule can be regarded as a momentum-based gradient-based descent which has been widely explored for optimizer learning problems [Hospedales et al., 2020].

Overall, the trainable components of the 4DVarNet scheme comprise: operators g and h , prior Φ , LSTM cell \mathcal{R} , and linear mapping \mathcal{L} . This amounts to a total number of parameters to be trained from data of about 1.4 M parameters for the considered case-study.

4.2 Learning setting

We benefit from the end-to-end feature of the considered 4DVarNet scheme to run a supervised strategy. It learns all trainable components with a view to optimizing the reconstruction performance. The training loss then combines reconstruction losses for SSH and SSC fields accounting respectively for the SSH and its gradient, the zonal and meridional components of current state $\mathbf{x}_{\text{SSC}} = (\mathbf{x}_u, \mathbf{x}_v)$, and the divergence of the SSC fields:

$$\mathcal{L}_{\nabla \text{SSH}} = \sum_i \alpha_{\text{SSH}} \|\mathbf{x}_{\text{SSH},i}^{\text{true}} - \widehat{\mathbf{x}}_{\text{SSH},i}\|^2 + \alpha_{\nabla \text{SSH}} \|\nabla \mathbf{x}_{\text{SSH},i}^{\text{true}} - \nabla \widehat{\mathbf{x}}_{\text{SSH},i}\|^2 \quad (9)$$

$$\mathcal{L}_{u,v} = \sum_i \|\mathbf{x}_{u,i}^{\text{true}} - \widehat{\mathbf{x}}_{u,i}\|^2 + \|\mathbf{x}_{v,i}^{\text{true}} - \widehat{\mathbf{x}}_{v,i}\|^2 \quad (10)$$

$$\mathcal{L}_{\text{div}} = \sum_i \|\partial_x \mathbf{x}_{u,i}^{\text{true}} + \partial_y \mathbf{x}_{v,i}^{\text{true}} - \partial_x \widehat{\mathbf{x}}_{u,i} - \partial_y \widehat{\mathbf{x}}_{v,i}\|^2 \quad (11)$$

where superscript ^{true} (resp. $\widehat{\cdot}$) refers to the true (resp. reconstructed) SSH or SSC fields. As proposed in [Fablet et al., 2021b], we complement these training losses with additional regularisation terms

$$\mathcal{L}_{\Phi} = \sum_i \|\mathbf{x}_i^{\text{true}} - \Phi(\mathbf{x}_i^{\text{true}})\|^2 + \sum_i \|\widehat{\mathbf{x}}_i - \Phi(\widehat{\mathbf{x}}_i)\|^2 \quad (12)$$

These regularisation terms better constrain the training of prior Φ .

Overall, we implement the 4DVarNet scheme and the associated learning strategy within Pytorch framework. We use Adam as optimizer with a fixed learning rate of 10^{-3} . After a first training procedure over 200 epochs, we fine-tune the best model over the validation dataset over 200 more epochs. The Pytorch code of our implementation is open source [Febvre et al., 2022].

²We refer the reader to [Fablet et al., 2022] for a detailed description of this two-scale decomposition of the SSH component of the state \mathbf{x} .

Approach	Data used	$\lambda_{x,u}$ ($^{\circ}$)	$\lambda_{x,v}$ ($^{\circ}$)	$\lambda_{t,u}$ (d)	$\lambda_{t,v}$ (d)	$\tau_{u,v}$	τ_{vort}	τ_{div}	τ_{strain}
True SSH	SSH only	0.36	0.17	19.6	11.2	97.0%	96.3%	-1.0%	92.1%
DUACS	SSH only	1.72	1.24	12.4	11.6	83.7%	53.5%	-0.5%	24.8%
U-Net	SSH only	1.39	1.22	9.1	10.3	89.1%	72.3%	-3.0%	65.0%
	SSH-SST	1.33	0.90	4.0	4.2	92.6%	79.4%	19.5%	72.0%
4DVarNet (ours)	SSH only	0.9	0.7	4.3	5.6	94.0%	86.1%	12.1%	81.3%
	SSH-SST	0.76	0.61	2.7	2.5	97.4%	92.1%	46.9%	87.2%

Table 1: **Synthesis of the reconstruction performance of the benchmarked approaches:** we report the performance metrics of the benchmarked approaches for the reconstruction of image time series of sea surface currents from satellite data. We refer the reader to the main text for the description of the different metrics. We highlight in bold the best score.

4.3 Evaluation framework and benchmarked approaches

Our numerical experiments involve a quantitative evaluation of the reconstruction performance using metrics evaluated over the test dataset. We adapt the metrics introduced in [Le Guillou et al., 2020] for mapping SSH fields and geostrophic SSC fields³, especially:

- $\lambda_{t,u}$ and $\lambda_{t,v}$, the minimum time scale resolved in days for respectively the zonal and meridional velocities;
- $\lambda_{x,u}$ and $\lambda_{x,v}$, the minimum spatial scale resolved in degrees for respectively the zonal and meridional velocities.

As described in [Le Guillou et al., 2020], these metrics rely on a spectral analysis. We also evaluate the reconstruction performance in terms of explained variance, respectively:

- $\tau_{u,v}$, the explained variance for the reconstructed SSC;
- τ_{vort} , the explained variance for the vorticity of the reconstructed SSC;
- τ_{div} , the explained variance for the divergence of the reconstructed SSC;
- τ_{strain} , the explained variance for the strain of the reconstructed SSC [Balwada et al., 2021, Okubo, 1970, Weiss, 1991].

The last three metrics characterize the extent to which the reconstructed SSC capture the local deformation tensor of the true velocity fields. Numerically, the computation of the vorticity, divergence, and strain combines a Gaussian filtering and finite difference approximation of the first-order derivatives.

Our numerical experiments evaluate two configurations of the proposed 4DVarNet framework: one using only SSH observation data and the other one exploiting SST-SSH synergies. For benchmarking purposes, we perform a quantitative comparison with respect to the SSH-derived sea surface currents from the true SSH fields and optimally-interpolated DUACS ones [Taburet et al., 2019] using the geostrophic approximation introduced in Section 2. We also evaluate direct learning-based inversion schemes based on U-Net architectures [Cicek et al., 2016] to directly map observation data to SSC fields either considering only SSH observation data or jointly SSH and SST observation data.

5 Results

In this Section, we report the considered numerical experiments for the evaluation of the proposed 4DVarNet schemes for the reconstruction of sea surface currents.

Synthesis of the benchmarking experiments: Tab. 1 compares the performance of the benchmarked schemes. DUACS SSH-derived geostrophic currents provide a baseline performance with reconstruction score in line with those reported for the metrics considered for SSH mapping [Fablet et al., 2022, Le Guillou et al., 2020] with resolved space-time scales above 1° and 10 days. This baseline accounts for more than 80% of the variance of the total current and about 50% of its vorticity and 25% of its strain. The two 4DVarNet schemes clearly outperform this reconstruction performance with

³We refer the reader to the following link for the detailed presentation of the evaluation experiment and benchmarked approaches https://github.com/ocean-data-challenges/2020a_SSH_mapping_NATL60

resolved space-time scales below 1° and 7 days. The relative improvement is particularly significant when exploiting SSH-SST synergies, especially for resolved time scales below 3 days. Interestingly, with this 4DVarNet configuration, the metrics for the explained variance of the different fields are better than those of the SSH-derived currents using the true SSH. In this respect, the poorly-resolved time scales of the latter are indicators of the relative contribution of the ageostrophic component of the total currents. Both 4DVarNet configurations learn to correct geostrophic velocities to better recover these temporal features. Though the configuration using only altimetry data only recover on average 12% of the divergent component of the SSC, the SSH-SST synergies captured by the 4DVarNet through the multimodal observation term in variational formulation (7) greatly improve the ability to retrieve a significant fraction of this divergent component (here, $\approx 47\%$ on average). The reported relative improvement greater than 30% for most of the performance metrics further highlights their contribution. This benchmarking experiment also clearly supports the relevance of 4DVarNet schemes compared with direct learning-based inversion schemes using off-the-shelf deep learning architecture. For instance, we report for all metrics a better reconstruction performance of the 4DVarNet scheme using only altimetry data than that of a direct UNet-based inversion with altimetry and SST inputs.

Fig. 3 further illustrates these results through the reconstructed fields on November 12th 2013. This example stresses some strengthening of the sea surface current along the main meander compared with the SSH-derived geostrophic velocities. This is captured by 4DVarNet reconstruction using SSH-SST synergies. They also illustrate the improvement regarding fine-scale patterns which are smoothed by DUACS baseline. The comparison of the vorticity also indicates some correction of the SSH-derived estimation which is revealed by 4DVarNet scheme. Visually, the reconstructed divergence using 4DVarNet schemes recover important features of the true divergence, though finer-scale patterns are lost, which is in line with the performance metrics reported in Tab. 1.

Data	$\lambda_{x,u}$ ($^\circ$)	$\lambda_{x,v}$ ($^\circ$)	$\lambda_{t,u}$ (d)	$\lambda_{t,v}$ (d)	$\tau_{u,v}$	τ_{vort}	τ_{div}	τ_{strain}
NAlt	1.5	1.0	6.5	6.4	91.7%	79.0%	8.8%	72.7%
NAlt+SWOT	0.9	0.7	4.3	5.6	94.0%	86.1%	12.1%	81.3%
NALT+SST	0.81	0.62	2.6	2.5	97.1%	90.8%	46.3%	85.0%
NAlt+SWOT+SST	0.76	0.61	2.7	2.5	97.4%	92.1%	46.9%	87.2%

Table 2: **Impact of SWOT and SST data onto the reconstruction performance w.r.t. a baseline using only nadir altimetry data:** we evaluate the performance metrics over the tests dataset for the trained 4DVarNet schemes reported in Tab.1 when considering nadir altimetry only (NAlt), nadir and wide-swath SWOT (NAlt+SWOT) altimetry combined or not with SST data in the proposed multimodal framework. Bold values show the highest skill.

Impact of SWOT data: We analyse in Tab. 2 how SWOT data contribute to the reconstruction of sea surface currents. For the trained 4DVarNet models considered in Tab. 1, we evaluate their reconstruction performance when considering only nadir altimetry data rather than nadir and SWOT altimetry data as used in the baseline configuration. These results support the relevance of wide-swath altimetry data to improve the reconstruction of sea surface currents. We report for instance a relative improvement greater than 25% for both $\tau_{u,v}$, τ_{vort} and τ_{strain} metrics and improved resolved time scales of 4.3 days vs. 6.5 days for the zonal velocity. When exploiting SSH-SST synergies, we also observed some improvement though smaller. We observe the greatest relative improvement between 10% and 15% for $\tau_{u,v}$, τ_{vort} and τ_{strain} metrics. This emphasizes for the considered case-study that SST fields bring most of the relevant information to retrieve the fine-scale patterns of sea surface currents.

Impact of the spatial resolution of the SST data: As the spatial resolution of satellite-derived SST products depends both on the satellite sensors as well as on the atmospheric conditions, we evaluate here the impact of the spatial resolution of the SST fields onto the reconstruction performance. From the trained multimodal 4DVarNet, we fine-tune multimodal 4DVarNet models using coarsened and subsampled versions of the original SST fields for spatial resolutions ranging from $1/10^\circ$ to $1/2^\circ$. We compare in Tab.3 the performance metrics of these models. As expected, the lower the resolution of the SST, the lower the performance. When considering SST data with a $1/2^\circ$ resolution, we only significantly improve the reconstruction of the divergent component of the SSC (25.4% vs. 12% when using only altimetry data). From a $1/4^\circ$ resolution, we report an improvement for all metrics, which is more noticeable for the resolved time scales. This is of key interest for the application to real microwave SST data [O’Carroll et al., 2019]. Besides, the clear gain issued from higher-resolution data also supports the potential of multispectral satellite sensors. Overall, Tab.3 suggests that the key SST features used to inform sea surface currents relate to horizontal scales between $1/20^\circ$ and $1/2^\circ$.

Analysis of the reconstruction error: We further analyse the reconstruction error and illustrate in Fig. 4 the time-averaged mean square error of the total sea surface current over the considered dataset from October 20th 2012 to December 4th 2012 for the trained 4DVarNet scheme exploiting SSH-SST synergies. We also report the time-averaged

SST resolution	$\lambda_{x,u}$ ($^{\circ}$)	$\lambda_{x,v}$ ($^{\circ}$)	$\lambda_{t,u}$ (d)	$\lambda_{t,v}$ (d)	$\tau_{u,v}$	τ_{vort}	τ_{div}	τ_{strain}
$1/20^{\circ}$	0.76	0.61	2.7	2.5	97.4%	92.1%	46.9%	87.2%
$1/10^{\circ}$	0.81	0.62	3.0	2.6	96.9%	90.8%	41.8%	85.1%
$1/5^{\circ}$	0.87	0.68	3.0	4.4	96.2%	89.0%	37.3%	83.2%
$1/4^{\circ}$	0.90	0.70	3.0	3.5	95.6%	87.4%	30.0%	81.5%
$1/2^{\circ}$	0.92	0.82	4.3	6.3	94.3%	85.3%	25.4%	80.0%

Table 3: **Impact of the spatial resolution of the SST observations:** we report the performance metrics of the proposed 4DVarNet models using SSH-SST synergies for SST observations with different spatial resolutions from $1/20^{\circ}$ to $1/2^{\circ}$. We refer the reader to the main text for the description of the different metrics. Bold values show the highest skills.

strain of the true velocities along with the time-averaged amplitude of horizontal SST gradients. We observe a better match between error and strain patterns. Quantitatively, the time-averaged strain explains about 60% of the time-averaged error over the test dataset. We reach similar correlation statistics for the reconstructed strain as expected from the visual similarity between the true and reconstructed strain depicted in Fig. 3.

We know that the strain highlights regions of frontogenesis or gradient strengthening [Balwada et al., 2021, Okubo, 1970, Weiss, 1991]. It could also be demonstrated that it leads to velocity error growth (Appendix). This is also consistent with kinetic energy transfer occurring due to the strain of the flow [Sévellec et al., 2022]. Here we hypothesized that regions of significant error growth (i.e., strain active regions) are more difficult to reconstruct due to their chaotic nature (i.e, small disturbances will become a significant signal). However we do not expect a perfect relation between surface strain and velocity error growth (and so velocity reconstruction error) since other terms, such as viscous terms or sub-surface pressure gradients, also control the velocities, and can become sources of error growth. Interestingly, this analysis is similar for the true strain and the reconstructed one, which could provide a proxy for the quantification of the uncertainty of the reconstruction using 4DVarNet schemes.

6 Discussion

This study has introduced a 4DVarNet deep learning scheme, backed on a variational data assimilation formulation, for the reconstruction of sea surface currents from satellite-derived SSH and SST observations. Our numerical experiments support the relevance of this learning-based approach over state-of-the-art schemes to retrieve finer-scale sea surface dynamics (typically 0.5 - 0.7° and 3 days for the resolved space-time scales), including a significant fraction of the ageostrophic component of the total current (about 47% of the divergence of the SSC). The good skill of 4DVarNet in the reconstruction of the horizontal divergence of the flow makes it particularly relevant for tracking surface/buoyant pollutant concentration (for which convergence regions act as attractors [Sévellec et al., 2017]). It is also important for the hypothetic reconstruction of vertical velocities (which vertical gradient is directly related to the horizontal divergence of the flow), with all their dynamical consequences for the export of nutrients, heat, and carbon, for instance. We have also hypothesized, through theoretical arguments, and shown the relation between the flow strain and the error of the reconstructed horizontal velocities. This suggests that strain active regions are good candidates for intense monitoring if one aims to better reconstruct horizontal velocities. We further discuss our contributions according to the following aspects: the monitoring of sea surface velocities, deep learning inversions for unobserved upper ocean dynamics and multimodal synergies for ocean monitoring and forecasting.

Reconstruction of sea surface velocities: Satellite altimetry plays a major role in our ability to monitor sea surface dynamics on a global to local scale. Through the direct measurement of the sea level anomaly, it delivers an estimation of the geostrophic component of sea surface velocities [Chelton et al., 2001]. As the scarce sampling of the sea surface by nadir altimeters limits our ability to retrieve dynamical features below $\approx 1^{\circ}$ and 10 days, research effort has been undertaken to observe and reconstruct finer-scale dynamics. In this context, upcoming swide-swath altimetry mission SWOT [Gaultier et al., 2015] will provide the first snapshots of the sea surface height down to a $1/10^{\circ}$ spatial resolution. Similarly to nadir altimeters, it will only directly inform the geostrophic component of sea surface velocities. Numerous studies (e.g., [Baaklini et al., 2021, Mahadevan and Tandon, 2006]) have evidenced the key role of ageostrophic dynamics in the mesoscale-to-submesoscale range. This has motivated a large research effort towards the exploitation of other observation sources, alone or combined with satellite altimetry, to retrieve sea surface dynamics, including among others SST [Fablet et al., 2018, Isern-Fontanet et al., 2014, Rio et al., 2016], Ocean Colour [Ciani et al., 2021], sea surface drifters [Baaklini et al., 2021, Sun et al., 2022], and SAR observations [Chapron et al., 2005]. From a methodological point of view, we may distinguish three main categories of approaches: optimal interpolation schemes [Cressie and Wikle, 2015, Taburet et al., 2019], data-driven approaches [Fablet et al., 2017, 2022, Manucharyan et al.,

2021], and data assimilation scheme using OGCM [Benkiran et al., 2021, Fujii et al., 2019] or QG dynamical priors [Le Guillou et al., 2020, Ubelmann et al., 2014]. The proposed 4DVarNet scheme benefits, on the one hand, from a variational data assimilation formulation to make explicit observation and dynamical priors, especially the expected though unknown relationship between SST and SSC features, and, on the other hand, from the computational efficiency of deep learning schemes, to learn uncalibrated terms and solvers from data in an end-to-end manner. This seems particularly promising to make the most of available multi-source observation datasets for the reconstruction of sea surface currents. Our study supports the ability to retrieve finer-scale patterns than currently achieved by operational products. While our study points out the added-value of wide-swath altimetry data, it suggests that ageostrophic components can be revealed by learning-based schemes from other sea surface tracers sampled at higher-resolution as illustrated with SST fields in our study. This likely relates to specific dynamical regimes in play in the Gulf Stream region [McWilliams et al., 2019, Reul et al., 2014]. Key challenges for future work include the exploration of the proposed framework for the variety of dynamical regimes exhibited by upper ocean dynamics as well as the transfer from OSSE to real observation dataset. The extension to other observation datasets such as drifter trajectories [Baaklini et al., 2021, Sun et al., 2022], SAR observations, as well as multispectral satellite sensors [Barnes et al., 2021, Tilstone et al., 2021, Yurovskaya et al., 2019] also naturally arises as appealing research directions. Whereas our OSSE provides a noise-free idealized testbed, real altimetry observations involve both observation noises and high-frequency fine-scale geophysical signals, such as internal tides and internal gravity waves Arbic et al. [2010], Xu and Fu [2012]. Numerous studies support the potential robustness of deep learning schemes to noisy patterns, when the training dataset involves appropriate noise simulations Shorten and Chin [2019]. The availability of realistic tide-resolving submesoscale-permitting ocean simulations provides the basis to address these issues in a future work using the proposed framework. A more challenging task will be the separation of tide-related and tide-free motions at sea surface, which could benefit from an extended version of the proposed neural approach.

Deep learning inversion for unobserved upper ocean dynamics: Our study further supports the potential for deep learning approaches to reconstruct unobserved or partially-observed variables or processes from available satellite-derived and/or *in situ* observation datasets. The reported case-study for horizontal sea surface currents is in line with recent studies addressing ocean processes, such as ocean eddy heat fluxes [George et al., 2021], tide-related features [Wang et al., 2022], plankton dynamics [Martinez et al., 2020]... The underlying assumption is that deep learning can disentangle the features associated with a given process in the observations of a tracer. In this context, classic data assimilation scheme requires defining explicitly the observations and dynamical operator in play in the underlying state-space formulation (5). Regarding upper ocean dynamics, this generally resorts to considering some discretization of the primitive equations and identity observation operators for ocean state variables and ocean-atmosphere interactions. The complexity of the inversion problem may hinder the ability of these schemes to retrieve fine-scale dynamics when dealing with a poorly-constrained observation setting as with the inversion of ocean dynamics from satellite-derived sea surface observations. By contrast, the proposed deep learning scheme focuses only on the ocean variable of interest, here observed and targeted sea surface variables. Through this learning paradigm, we reduce the complexity of the inversion problem and explore the complex relationships exhibited by sea surface tracers governed by upper ocean dynamics. We believe this approach to be generic and to show a potential to improve our understanding and monitoring of upper ocean dynamics which will remain scarcely observed.

OSSEs and Deep Learning to Bridge ocean modeling and multimodal ocean remote sensing: We may also regard the proposed deep learning schemes as alternative means to bridge ocean modeling and ocean observation. Through the combination of simulation dataset for ocean dynamics and observing systems, OSSE settings [Boukabara et al., 2018, Fujii et al., 2019] have been widely exploited as means to assess the potential impact of new observing systems to improve the reconstruction and/or forecasting of ocean dynamics. OSSEs in the context of the upcoming SWOT mission fall into this category to evaluate the added-value of wide-swath altimetry data to inform upper ocean dynamics [Benkiran et al., 2021, Ubelmann et al., 2014], as further supported by this study. More recently, OSSEs have provided benchmarking frameworks to intercompare the performance of different approaches for the same task such as space-time interpolation problems for sea surface dynamics [Fablet et al., 2022, Le Guillou et al., 2020, Fujii et al., 2019, Vient et al., 2021]. As illustrated here, when dealing with unobserved or scarcely observed processes, OSSEs also provide means to train a model from simulation datasets with a view to applying this model to real datasets. Previous learning-based studies dedicated to the reconstruction of ocean’s interior processes, such as for instance the primary production [Puissant et al., 2021] and deep geostrophic currents [Manucharyan et al., 2021], provide such examples. These studies generally learn a mapping from observed gap-free sea surface tracers to the targeted ocean state dynamics. Our study supports the ability to further extend this approach to reconstruction or mapping objectives from irregularly-sampled observations. The applicability of this general framework to real observation datasets clearly depends on the quality of both the numerical simulations of ocean dynamics and of the simulations of the observing systems. As such, it advocates to pursue joint research effort into these simulation issues along with the design and evaluation of deep learning approaches. We believe these aspects to be critical for the development of multimodal observing systems combining satellite-derived observations and *in situ* data including among others sea surface drifters [Baaklini et al.,

2021, Sun et al., 2022], argo profiles [Cossarini et al., 2019, Roemmich et al., 2019], and underwater acoustics data [Storto et al., 2020, 2021]...

Appendix: Velocity error growth

Starting from the momentum and nondivergence equations [described in (1)] but splitting the velocity (and pressure and viscous terms) in a targeted truth and a small error ($X = \bar{X} + X'$ with $|\bar{X}| \ll |X'|$, where X is any variable) we have:

$$D_t u' - f v' = -u' \partial_x \bar{u} - v' \partial_y \bar{u} - w' \partial_z \bar{u} - \frac{1}{\rho_0} \partial_x P' + \mathcal{F}'_x, \quad (13a)$$

$$D_t v' + f u' = -u' \partial_x \bar{v} - v' \partial_y \bar{v} - w' \partial_z \bar{v} - \frac{1}{\rho_0} \partial_y P' + \mathcal{F}'_y. \quad (13b)$$

$$0 = -\frac{1}{\rho_0} \partial_z P' - \frac{g}{\rho_0} \rho', \quad (13c)$$

$$\partial_x u' + \partial_y v' + \partial_z w' = 0. \quad (13d)$$

So that error growth reads:

$$\begin{aligned} D_t (u'^2 + v'^2) = & -(u', v') \begin{pmatrix} \partial_x \bar{u} & \partial_y \bar{u} \\ \partial_x \bar{v} & \partial_y \bar{v} \end{pmatrix} \begin{pmatrix} u' \\ v' \end{pmatrix} \\ & - u' w' \partial_z \bar{u} - v' w' \partial_z \bar{v} - \frac{g}{\rho_0} w' \rho' \\ & - \frac{1}{\rho_0} [\partial_x (u' P') + \partial_y (v' P') + \partial_z (w' P')] + (u' \mathcal{F}'_x + v' \mathcal{F}'_y), \end{aligned} \quad (14)$$

where the left handside is the evolution of the error (or error growth), the first line of the right handside is the horizontal transfer of momentum error, the second line of the right handside is the baroclinic transfer of momentum and density errors, and the third line of the right handside is the work of the pressure and viscous force error. Here the horizontal transfer of momentum error is a scalar product of the erroneous velocities applied to the operator of horizontal targeted-truth-velocity gradient. This could be transformed as:

$$\begin{aligned} (u', v') \Sigma \begin{pmatrix} u' \\ v' \end{pmatrix} &= \begin{pmatrix} \partial_x \bar{u} & \partial_y \bar{u} \\ \partial_x \bar{v} & \partial_y \bar{v} \end{pmatrix} \begin{pmatrix} u' \\ v' \end{pmatrix}, \\ &= \frac{1}{2} (u', v') \begin{pmatrix} \Delta + \sigma_n & \sigma_s + \zeta \\ \sigma_s - \zeta & \Delta - \sigma_n \end{pmatrix} \begin{pmatrix} u' \\ v' \end{pmatrix}, \\ &= \frac{1}{2} (u', v') \begin{pmatrix} \Delta + \sigma_n & \sigma_s \\ \sigma_s & \Delta - \sigma_n \end{pmatrix} \begin{pmatrix} u' \\ v' \end{pmatrix}, \end{aligned} \quad (15)$$

where $\Delta = \partial_x \bar{u} + \partial_y \bar{v}$ is the divergence, $\zeta = \partial_x \bar{v} - \partial_y \bar{u}$ is the horizontal vorticity, $\sigma_n = \partial_x \bar{u} - \partial_y \bar{v}$ is the normal strain (or stretching), and $\sigma_s = \partial_x \bar{v} + \partial_y \bar{u}$ is the shear strain (or shearing). This last expression shows the symmetric part of the gradient deformation operator, which is virtually equivalent to the one used for tracer gradient growth [Balwada et al., 2021] in the Okubo-Weiss framework of frontogenesis [Okubo, 1970, Weiss, 1991]. It is interesting to note that here the horizontal vorticity (ζ) does not contribute to the error growth, though. Σ can be diagonalized to show the natural growth of the error, which leads to the pair of eigenvalues: $\lambda_{\pm} = \Delta/2 \pm \sigma/2$, where σ is the strain (such as $\sigma^2 = \sigma_n^2 + \sigma_s^2$). Since the horizontal flow is largely strain dominated, this shows that the error growth is controlled by the strain. This result is consistent with energy transfer consideration suggesting the transfer from the mean state (here the targeted-truth) to the eddy field (here the error) following the strain of the flow [Sévellec et al., 2022]. However note that the total error growth will also be affected by baroclinic error transfers and pressure and viscous work.

Acknowledgements

This work was supported by LEFE program (LEFE MANU and IMAGO projects IA-OAC and ARVOR, respectively), CNES (OSTST DUACS-HR and SWOT ST DIEGO) and ANR Projects Melody (ANR-19-CE46-0011) and OceaniX (ANR-19-CHIA-0016). It benefited from HPC and GPU resources from Azure (Microsoft Azure grant) and from GENCI-IDRIS (Grant 2021-101030).

References

- D.B. Chelton, J.C. Ries, B. J. Haines, L.-L. Fu, and P. S. Callahan. Satellite Altimetry. In A. Cazenave and L.-L. Fu, editors, *International Geophysics*, volume 69 of *Satellite Altimetry and Earth Sciences A Handbook of Techniques and Applications*. Academic Press, 2001.
- M. Ballarotta, C. Ubelmann, M.-I. Pujol, G. Taburet, F. Fournier, J.F. Legeais, Y. Faugère, A. Delepouille, D. Chelton, and N. Picot. On the resolutions of ocean altimetry maps. *Ocean Science*, 15(4):1091–1109, 2019. doi:<https://doi.org/10.5194/os-15-1091-2019>.
- A. Mahadevan and A. Tandon. An analysis of mechanisms for submesoscale vertical motion at ocean fronts. *Ocean Modelling*, 14(3):241–256, 2006. ISSN 1463-5003. doi:10.1016/j.ocemod.2006.05.006.
- G. Baaklini, L. Issa, M. Fakhri, J. Brajard, G. Fifani, M. Menna, I. Taupier-Letage, A. Bosse, and L. Mortier. Blending drifters and altimetric data to estimate surface currents: Application in the Levantine Mediterranean and objective validation with different data types. *Ocean Mod.*, 166:101850, 2021. doi:10.1016/j.ocemod.2021.101850.
- L. Sun, Stephen G. Penny, and M. Harrison. Impacts of the Lagrangian Data Assimilation of Surface Drifters on Estimating Ocean Circulation during the Gulf of Mexico Grand Lagrangian Deployment. *Mont. Weath. Rev.*, 150(4): 949–965, 2022. doi:10.1175/MWR-D-21-0123.1.
- Takaya Uchida, Julien Le Sommer, Charles Stern, Ryan P. Abernathy, Chris Holdgraf, Aurélie Albert, Laurent Brodeau, Eric P. Chassignet, Xiaobiao Xu, Jonathan Gula, Guillaume Roullet, Nikolay Koldunov, Sergey Danilov, Qiang Wang, Dimitris Menemenlis, Clément Bricaud, Brian K. Arbic, Jay F. Shriver, Fangli Qiao, Bin Xiao, Arne Biastoch, René Schubert, Baylor Fox-Kemper, William K. Dewar, and Alan Wallcraft. Cloud-based framework for inter-comparing submesoscale-permitting realistic ocean models. *Geoscientific Model Development*, 15(14): 5829–5856, 2022. doi:10.5194/gmd-15-5829-2022.
- Ana B. Villas Boas, Fabrice Ardhuin, Alex Ayet, Mark A. Bourassa, Peter Brandt, Bertrand Chapron, Bruce D. Cornuelle, J. T. Farrar, Melanie R. Fewings, Baylor Fox-Kemper, Sarah T. Gille, Christine Gommenginger, Patrick Heimbach, Momme C. Hell, Qing Li, Matthew R. Mazloff, Sophia T. Merrifield, Alexis Mouche, Marie H. Rio, Ernesto Rodriguez, Jamie D. Shutler, Aneesh C. Subramanian, Eric J. Terrill, Michel Tsamados, Clement Ubelmann, and Erik van Sebille. Integrated Observations of Global Surface Winds, Currents, and Waves: Requirements and Challenges for the Next Decade. *Frontiers in Marine Science*, 6, 2019.
- Fabrice Ardhuin, Peter Brandt, Lucile Gaultier, Craig Donlon, Alessandro Battaglia, François Boy, Tania Casal, Bertrand Chapron, Fabrice Collard, Sophie Cravatte, Jean-Marc Delouis, Erik De Witte, Gerald Dibarbouré, Geir Engen, Harald Johnsen, Camille Lique, Paco Lopez-Dekker, Christophe Maes, Adrien Martin, Louis Marié, Dimitris Menemenlis, Frederic Nouguier, Charles Peureux, Pierre Rampal, Gerhard Ressler, Marie-Helene Rio, Bjorn Rommen, Jamie D. Shutler, Martin Suess, Michel Tsamados, Clement Ubelmann, Erik van Sebille, Martin van den Oever, and Detlef Stammer. SKIM, a Candidate Satellite Mission Exploring Global Ocean Currents and Waves. *Frontiers in Marine Science*, 6, 2019. ISSN 2296-7745. URL <https://www.frontiersin.org/articles/10.3389/fmars.2019.00209>.
- A.M. Moore, M.J. Martin, S. Akella, H.G. Arango, M. Balmaseda, L. Bertino, S. Ciavatta, B. Cornuelle, J. Cummings, S. Frolov, P. Lermusiaux, P. Oddo, P.R. Oke, A. Storto, A. Teruzzi, A. Vidard, and A.T. Weaver. Synthesis of Ocean Observations Using Data Assimilation for Operational, Real-Time and Reanalysis Systems: A More Complete Picture of the State of the Ocean. *Frontiers in Marine Science*, 6, 2019.
- Andrea Storto, Aida Alvera-Azcarate, Magdalena A. Balmaseda, Alexander Barth, Matthieu Chevallier, Francois Counillon, Catia M. Domingues, Marie Drevillon, Yann Drillet, Gaël Forget, Gilles Garric, Keith Haines, Fabrice Hernandez, Doroteaciro Iovino, Laura C. Jackson, Jean-Michel Lellouche, Simona Masina, Michael Mayer, Peter R. Oke, Stephen G. Penny, K. Andrew Peterson, Chunxue Yang, and Hao Zuo. Ocean Reanalyses: Recent Advances and Unsolved Challenges. *Frontiers in Marine Science*, 6, 2019. ISSN 2296-7745. URL <https://www.frontiersin.org/articles/10.3389/fmars.2019.00418>.
- G. Taburet, A. Sanchez-Roman, M. Ballarotta, M.-I. Pujol, F.F. Legeais, F. Fournier, Y. Faugere, and G. Dibarbouré. DUACS DT2018: 25 years of reprocessed sea level altimetry products. *Ocean Sci.*, page 18, 2019. doi:10.5194/os-15-1207-2019.
- M. Benkiran, G. Ruggiero, E. Greiner, P.-Y. Le Traon, E. Rémy, J.M. Lellouche, R. Bourdallé-Badie, Y. Drillet, and B. Tchonang. Assessing the Impact of the Assimilation of SWOT Observations in a Global High-Resolution Analysis and Forecasting System Part 1: Methods. *Frontiers in Marine Science*, 8, 2021. doi:10.3389/fmars.2021.691955.
- Y. Fujii, E. Rémy, H. Zuo, P. Oke, George Halliwell, Florent Gasparin, Mounir Benkiran, Nora Loose, James Cummings, Jiping Xie, Yan Xue, Shuhei Masuda, Gregory C. Smith, Magdalena Balmaseda, Cyril Germineaud, Daniel J. Lea, Gilles Larnicol, Laurent Bertino, Antonio Bonaduce, Pierre Brasseur, Craig Donlon, Patrick Heimbach, YoungHo

- Kim, Villy Kourafalou, Pierre-Yves Le Traon, Matthew Martin, Shastri Paturi, Benoit Tranchant, and N. Usui. Observing System Evaluation Based on Ocean Data Assimilation and Prediction Systems: On-Going Challenges and a Future Vision for Designing and Supporting Ocean Observational Networks. *Front. Mar. Sc.*, 6, 2019. doi:10.3389/fmars.2019.00417.
- D. Ciani, E. Charles, B. Buongiorno Nardelli, M.-H. Rio, and R. Santoleri. Ocean Currents Reconstruction from a Combination of Altimeter and Ocean Colour Data: A Feasibility Study. *Rem. Sens.*, 13(12):2389, 2021. doi:10.3390/rs13122389.
- J. Isern-Fontanet, B. Chapron, G. Lapeyre, and P. Klein. Potential use of microwave sea surface temperatures for the estimation of ocean currents. *Geophysical Res. Lett.*, 33(L24608), 2006. URL doi : 10.1029/2006GL027801.
- A. Alvera-Azcárate, A. Barth, J.-M. Beckers, and R. H. Weisberg. Multivariate reconstruction of missing data in sea surface temperature, chlorophyll, and wind satellite fields. *Journal of Geophysical Research: Oceans*, 112(C3), 2007. doi:10.1029/2006JC003660.
- R. Lguensat, P. Tandeo, P. Aillot, and R. Fablet. The Analog Data Assimilation. *Monthly Weather Review*, 2017.
- A. Barth, A. Alvera-Azcárate, M. Licer, and J.-M. Beckers. DINCAE 1.0: a convolutional neural network with error estimates to reconstruct sea surface temperature satellite observations. *Geosci. Mod. Dev.*, 13(3):1609–1622, 2020. doi:10.5194/gmd-13-1609-2020.
- R. Fablet, M. M. Amar, Q. Febvre, M. Beauchamp, and B. Chapron. End-to-end physics-informed representation learning for satellite ocean remote sensing: applications to satellite altimetry and sea surface currents. In *ISPRS Ann. Photogram. Rem. Sens. Spat. Inf. Sc.*, volume V-3-2021, pages 295–302, 2021a. doi:10.5194/isprs-annals-V-3-2021-295-2021.
- R. Fablet, Q. Febvre, and B. Chapron. Multimodal 4DVarNets for the reconstruction of sea surface dynamics from SST-SSH synergies. *arXiv:2207.01372*, 2022. doi:10.48550/arXiv.2207.01372.
- T.M. George, G.E. Manucharyan, and A.F. Thompson. Deep learning to infer eddy heat fluxes from sea surface height patterns of mesoscale turbulence. *Nature Communications*, 12(1):800, 2021. doi:10.1038/s41467-020-20779-9.
- G. E. Manucharyan, L. Siegelman, and P. Klein. A Deep Learning Approach to Spatiotemporal Sea Surface Height Interpolation and Estimation of Deep Currents in Geostrophic Ocean Turbulence. *JAMES*, 13(1):e2019MS001965, 2021. doi:10.1029/2019MS001965.
- F. Sévellec, A. Colin de Verdière, and N. Kolodziejczyk. Global observations of deep ocean kinetic energy transfers. *submitted in J. Phys. Oceanogr.*, 2022.
- G. Evensen. *Data Assimilation*. Springer Berlin Heidelberg, 2009.
- A. Carrassi, M. Bocquet, L. Bertino, and G. Evensen. Data assimilation in the geosciences: An overview of methods, issues, and perspectives. *WIREs Climate Change*, 9(5):e535, 2018. doi:10.1002/wcc.535.
- N. Cressie and C.K. Wikle. *Statistics for Spatio-Temporal Data*. John Wiley & Sons, 2015.
- F. Le Guillou, S. Metref, E. Cosme, C. Ubelmann, M. Ballarotta, J. Le Sommer, and J. Verron. Mapping Altimetry in the Forthcoming SWOT Era by Back-and-Forth Nudging a One-Layer Quasigeostrophic Model. *J. Atmos. Ocean. Tech.*, 38:697 – 710, 2020. doi:10.1175/jtech-d-20-0104.1.
- C. Ubelmann, P. Klein, and L.-L. Fu. Dynamic Interpolation of Sea Surface Height and Potential Applications for Future High-Resolution Altimetry Mapping. *J. Atmos. Ocean. Tech.*, 32(1):177–184, 2014. doi:10.1175/JTECH-D-14-00152.1.
- S. Abdalla, A. Abdeh Kolahchi, O.B. Andersen, Helena Antich, Brian Arbic, Thomas Armitage, Sabine Arnault, Camila Artana, Giuseppe Aulicino, Nadia Ayoub, Sergei Badulin, Steven Baker, Chris Banks, Lifeng Bao, Silvia Barbetta, Bàrbara Barceló-Llull, François Barlier, Sujit Basu, Peter Bauer-Gottwein, Matthias Becker, Brian Beckley, Nicole Bellefond, Tatyana Belonenko, Mounir Benkiran, Touati Benkouider, Ralf Bennartz, Jérôme Benveniste, Nicolas Bercher, Muriel Berge-Nguyen, Joao Bettencourt, Fabien Blarel, Alejandro Blazquez, Denis Blumstein, Pascal Bonnefond, Franck Borde, Jérôme Bouffard, François Boy, Jean-Paul Boy, Cédric Brachet, Pierre Bresseur, Alexander Braun, Luca Brocca, David Brockley, Laurent Brodeau, Shannon Brown, Sean Bruinsma, Anna Bulczak, Sammie Buzzard, Madeleine Cahill, Stéphane Calmant, Michel Calzas, Stefania Camici, Mathilde Cancet, Hugues Capdeville, Claudia Cristina Carabajal, Loren Carrere, Anny Cazenave, Eric P. Chassignet, Prakash Chauhan, Selma Cherchali, Teresa Chereskin, Cecile Cheymol, Daniele Ciani, Paolo Cipollini, Francesca Cirillo, Emmanuel Cosme, Steve Coss, Yuri Cotroneo, David Cotton, Alexandre Couhert, Sophie Coutin-Faye, Jean-François Crétaux, Frederic Cyr, Francesco d’Ovidio, José Darrozes, Cedric David, Nadim Dayoub, Danielle De Staerke, Xiaoli Deng, Shailen Desai, Jean-Damien Desjonqueres, Denise Dettmering, Alessandro Di Bella, Lara Díaz-Barroso, Gerald Dibarboure, Habib Boubacar Dieng, Salvatore Dinardo, Henryk Dobslaw, Guillaume Dodet, Andrea Doglioli, Alessio Domeneghetti, David Donahue, Shenfu Dong, Craig Donlon, Joël Dorandeu, Christine Drezen, Mark Drinkwater,

- Yves Du Penhoat, Brian Dushaw, Alejandro Egado, Svetlana Erofeeva, Philippe Escudier, Saskia Esselborn, Pierre Exertier, Ronan Fablet, Cédric Falco, Sinead Louise Farrell, Yannice Faugere, Pierre Femenias, Luciana Fenoglio, Joana Fernandes, Juan Gabriel Fernández, Pascale Ferrage, Ramiro Ferrari, Lionel Fichen, Paolo Filippucci, Stylianos Flampouris, Sara Fleury, Marco Fornari, Rene Forsberg, Frédéric Frappart, Marie-laure Frery, Pablo Garcia, Albert Garcia-Mondejar, Julia Gaudelli, Lucile Gaultier, Augusto Getirana, Ferran Gibert, Artur Gil, Lin Gilbert, Sarah Gille, Luisella Giulicchi, Jesús Gómez-Enri, Laura Gómez-Navarro, Christine Gommenginger, Lionel Gourdeau, David Griffin, Andreas Groh, Alexandre Guerin, Raul Guerrero, Thierry Guinle, Praveen Gupta, Benjamin D. Gutknecht, Mathieu Hamon, Guoqi Han, Danièle Hauser, Veit Helm, Stefan Hendricks, Fabrice Hernandez, Anna Hogg, Martin Horwath, Martina Idzanovic, Peter Janssen, Eric Jeansou, Yongjun Jia, Yuanyuan Jia, Liguang Jiang, Johnny A. Johannessen, Masafumi Kamachi, Svetlana Karimova, Kathryn Kelly, Sung Yong Kim, Robert King, Cecile M. M. Kittel, Patrice Klein, Anna Klos, Per Knudsen, Rolf Koenig, Andrey Kostianoy, Alexei Kouraev, Raj Kumar, Sylvie Labroue, Loreley Selene Lago, Juliette Lambin, Léa Lasson, Olivier Laurain, Rémi Laxenaire, Clara Lázaro, Sophie Le Gac, Julien Le Sommer, Pierre-Yves Le Traon, Sergey Lebedev, Fabien Léger, B. Legresy, Frank Lemoine, Luc Lenain, Eric Leuliette, Marina Levy, John Lillibridge, Jianqiang Liu, William Llovel, Florent Lyard, Claire Macintosh, Eduard Makhoul Varona, Cécile Manfredi, Frédéric Marin, Evan Mason, Christian Massari, Constantin Mavrocordatos, Nikolai Maximenko, Malcolm McMillan, Thierry Medina, Angélique Melet, Marco Meloni, Stelios Mertikas, Sammy Metref, Benoit Meyssignac, Jean-François Minster, Thomas Moreau, Daniel Moreira, Yves Morel, Rosemary Morrow, John Moyard, Sandrine Mulet, Marc Naeije, Robert Steven Nerem, Hans Ngodock, Karina Nielsen, Jan Even Øie Nilsen, Fernando Niño, Carolina Nogueira Loddo, Camille Noûs, Estelle Obligis, Inès Otosaka, Michiel Otten, Berguzar Oztunali Ozbahceci, Roshin P. Raj, Rodrigo Paiva, Guillermina Paniagua, Fernando Paolo, Adrien Paris, Ananda Pascual, Marcello Passaro, Stephan Paul, Tamlin Pavelsky, Christopher Pearson, Thierry Penduff, Fukai Peng, Felix Perosanz, Nicolas Picot, Fanny Piras, Valerio Poggiali, Étienne Poirier, Sonia Ponce de León, Sergey Prants, Catherine Prigent, Christine Provost, M-Isabelle Pujol, Bo Qiu, Yves Quilfen, Ali Rami, R. Keith Raney, Matthias Raynal, Elisabeth Remy, Frédérique Rémy, Marco Restano, Annie Richardson, Donald Richardson, Robert Ricker, Martina Ricko, Eero Rinne, Stine Kildegaard Rose, Vinca Rosmorduc, Sergei Rudenko, Simón Ruiz, Barbara J. Ryan, Corinne Salaün, Antonio Sanchez-Roman, Louise Sandberg Sørensen, David Sandwell, Martin Saraceno, Michele Scagliola, Philippe Schaeffer, Martin G. Scharffenberg, Remko Scharroo, Andreas Schiller, Raphael Schneider, Christian Schwatke, Andrea Scozzari, Enrico Ser-giacomi, Frederique Seyler, Rashmi Shah, Rashmi Sharma, Andrew Shaw, Andrew Shepherd, Jay Shriver, C. K. Shum, Wim Simons, Sebastian B. Simonsen, Thomas Slater, Walter Smith, Saulo Soares, Mikhail Sokolovskiy, Laurent Soudarin, Ciprian Spatar, Sabrina Speich, Margaret Srinivasan, Meric Srokosz, Emil Stanev, Joanna Staneva, Nathalie Steunou, Julienne Stroeve, Bob Su, Yohanes Budi Sulistioadi, Debadatta Swain, Annick Sylvestre-baron, Nicolas Taburet, Rémi Tailleux, Katsumi Takayama, Byron Tapley, Angelica Tarpanelli, Gilles Tavernier, Laurent Testut, Praveen K. Thakur, Pierre Thibaut, LuAnne Thompson, Joaquín Tintoré, Céline Tison, Cédric Tourain, Jean Tournadre, Bill Townsend, Ngan Tran, Sébastien Trilles, Michel Tsamados, Kuo-Hsin Tseng, Clément Ubelmann, Bernd Uebbing, Oscar Vergara, Jacques Verron, Telmo Vieira, Stefano Vignudelli, Nadya Vinogradova Shiffer, Pieter Visser, Frederic Vivier, Denis Volkov, Karina von Schuckmann, Valerii Vuglinskii, Pierrick Vuilleumier, Blake Walter, Jida Wang, Chao Wang, Christopher Watson, John Wilkin, Josh Willis, Hilary Wilson, Philip Woodworth, Kehan Yang, Fangfang Yao, Raymond Zaharia, Elena Zakharova, Edward D. Zaron, Yongsheng Zhang, Zhongxiang Zhao, and Vadim Zinchenko. Altimetry for the future: Building on 25 years of progress. *Adv. Space Res.*, 68(2):319–363, 2021. doi:10.1016/j.asr.2021.01.022.
- S. Barthelemy, J. Brajard, L. Bertino, and F. Counillon. Super-resolution data assimilation. *arXiv:2109.08017*, 2021. doi:10.48550/arXiv.2109.08017.
- P. Boudier, A. Fillion, S. Gratton, and S. Gürol. DAN – An optimal Data Assimilation framework based on machine learning Recurrent Networks. *arXiv:2010.09694*, October 2020.
- M. Bocquet, J. Brajard, A. Carrassi, and L. Bertino. Bayesian inference of chaotic dynamics by merging data assimilation, machine learning and expectation-maximization. *Foundations of Data Science*, 2(1):55–80, 2020. doi:10.3934/fods.2020004.
- R. Fablet, B. Chapron, L. Drumetz, E. Memin, O. Pannekoucke, and F. Rousseau. Learning Variational Data Assimilation Models and Solvers. *JAMES*, 13(e2021MS002572), 2021b.
- M. Nonnenmacher and D.S. Greenberg. Deep Emulators for Differentiation, Forecasting, and Parametrization in Earth Science Simulators. *JAMES*, 13(7):e2021MS002554, 2021. doi:10.1029/2021MS002554.
- A. Ajayi, J. Le Sommer, E. Chassignet, J.-M. Molines, X. Xu, A. Albert, and E. Cosme. Spatial and Temporal Variability of the North Atlantic Eddy Field From Two Kilometric-Resolution Ocean Models. *J. Geophys. Res.*, 125(5):e2019JC015827, 2020. doi:10.1029/2019JC015827.
- G. Madec, R. Bourdalle-Badie, J. Chanut, E. Clementi, A. Coward, C. Ethe, D. Iovino, D. Lea, C. Levy, T. Lovato, N. Martin, S. Masson, S. Mocavero, C. Rousset, D. Storkey, S. Mueller, G. Nurser, M. Bell, G. Samson, P. Mathiot, F. Mele, and A. Moulin. NEMO ocean engine. *Tech. Report*, 2022. doi:10.5281/zenodo.6334656.

- L. Gaultier, C. Ubelmann, and L.-L. Fu. The Challenge of Using Future SWOT Data for Oceanic Field Reconstruction. *J. Atm. Ocean. Tech.*, 33(1):119–126, 2015. doi:10.1175/JTECH-D-15-0160.1.
- C. J. Donlon, M. Martin, J. Stark, J. Roberts-Jones, E. Fiedler, and W. Xindong. The Operational Sea Surface Temperature and Sea Ice Analysis (OSTIA) system. *Rem. Sens. Env.*, 116:140–158, 2012. doi:10.1016/j.rse.2010.10.017.
- A.G. O’Carroll, E.M. Armstrong, H.M. Beggs, M. Bouali, K.S. Casey, Gary K. Corlett, Prasanjit Dash, Craig J. Donlon, Chelle L. Gentemann, Jacob L. Høyer, Alexander Ignatov, Kamila Kabobah, Misako Kachi, Yukio Kurihara, Ioanna Karagali, Eileen Maturi, Christopher J. Merchant, Salvatore Marullo, Peter J. Minnett, Matthew Pennybacker, Balaji Ramakrishnan, RAAJ Ramsankaran, Rosalia Santoleri, Swathy Sunder, Stéphane Saux Picart, Jorge Vázquez-Cuervo, and Werenfrid Wimmer. Observational Needs of Sea Surface Temperature. *Front. Mar. Sc.*, 6, 2019. doi:10.3389/fmars.2019.00420.
- O. Cicek, A. Abdulkadir, S.S. Lienkamp, T. Brox, and O. Ronneberger. 3D U-Net: learning dense volumetric segmentation from sparse annotation. In *Proc. MICCAI*, pages 424–432, 2016.
- M. Beauchamp, Q. Febvre, H. Georgenthum, and R. Fablet. End-to-end neural interpolation of satellite altimetry data using 4DVarNet schemes. *Submitted to Geosc. Meth. Dev.*, 2022. doi:https://doi.org/10.5194/gmd-2022-241.
- T. Hospedales, A. Antoniou, P. Micaelli, and A. Storkey. Meta-learning in neural networks: A survey. *arXiv:2004.05439*, 2020.
- Q. Febvre, M. Beauchamp, H. Georgenthum, and R. Fablet. Pytorch 4DVarNet code for the reconstruction of sea surface currents from SSH and SST data, 2022. doi:10.5281/zenodo.7186323.
- D. Balwada, Q. Xiao, S. Smith, R. Abernathy, and A.R. Gray. Vertical Fluxes Conditioned on Vorticity and Strain Reveal Submesoscale Ventilation. *J. Phys. Ocean.*, 51(9):2883–2901, 2021. doi:10.1175/JPO-D-21-0016.1.
- A. Okubo. Horizontal dispersion of floatable particles in the vicinity of velocity singularities such as convergences. *Deep Sea Res.*, 17(3):445–454, 1970.
- J. Weiss. The dynamics of enstrophy transfer in two-dimensional hydrodynamics. *Physica D: Nonlin. Phen.*, 48(2): 273–294, 1991.
- F. Sévellec, A. Colin de Verdière, and M. Ollitrault. Evolution of intermediate water masses based on argo float displacement. *J. Phys. Oceanogr.*, 47:1569–1586, 2017.
- R. Fablet, J. Verron, B. Moure, B. Chapron, and A. Pascual. Improving Mesoscale Altimetric Data From a Multitracer Convolutional Processing of Standard Satellite-Derived Products. *IEEE TGRS*, 56(5):2518–2525, 2018. doi:10.1109/TGRS.2017.2750491.
- J. Isern-Fontanet, M. Shinde, and C. Andersson. On the Transfer Function between Surface Fields and the Geostrophic Stream Function in the Mediterranean Sea. *J. Phys. Ocean.*, 44(5):1406–1423, 2014. doi:10.1175/JPO-D-13-0186.1.
- M.-H. Rio, R. Santoleri, R. Bourdalle-Badie, A. Griffa, L. Piterbarg, and G. Taburet. Improving the Altimeter-Derived Surface Currents Using High-Resolution Sea Surface Temperature Data: A Feasibility Study Based on Model Outputs. *J. Atm. Ocean. Tech.*, 33(12):2769–2784, 2016. doi:10.1175/JTECH-D-16-0017.1.
- B. Chapron, F. Collard, and F. Ardhuin. Direct measurements of ocean surface velocity from space: Interpretation and validation. *J. Geophys. Res.*, 110, 2005. doi:10.1029/2004JC002809.
- R. Fablet, P. H. Viet, and R. Lguensat. Data-Driven Models for the Spatio-Temporal Interpolation of Satellite-Derived SST Fields. *IEEE Trans. on Computational Imaging*, 3(4):647–657, 2017. doi:10.1109/TCI.2017.2749184.
- J.C. McWilliams, J. Gula, and M.J. Molemaker. The Gulf Stream North Wall: Ageostrophic Circulation and Frontogenesis. *Journal of Physical Oceanography*, 49(4):893–916, 2019. doi:10.1175/JPO-D-18-0203.1.
- N. Reul, B. Chapron, T. Lee, C. Donlon, J. Boutin, and G. Alory. Sea surface salinity structure of the meandering Gulf Stream revealed by SMOS sensor. *Geophysical Research Letters*, 41(9):3141–3148, 2014. doi:10.1002/2014GL059215.
- B.B. Barnes, C. Hu, S.W. Bailey, N. Pahlevan, and B.A. Franz. Cross-calibration of MODIS and VIIRS long near infrared bands for ocean color science and applications. *Rem. Sens. Env.*, 260:112439, 2021. ISSN 0034-4257. doi:10.1016/j.rse.2021.112439.
- G.H. Tilstone, S. Pardo, G. Dall’Olmo, R.J.W. Brewin, F. Nencioli, D. Dessailly, E. Kwiatkowska, T. Casal, and C. Donlon. Performance of Ocean Colour Chlorophyll a algorithms for Sentinel-3 OLCI, MODIS-Aqua and Suomi-VIIRS in open-ocean waters of the Atlantic. *Rem. Sens. Env.*, 260:112444, 2021. doi:10.1016/j.rse.2021.112444.
- M. Yurovskaya, V. Kudryavtsev, B. Chapron, and F. Collard. Ocean surface current retrieval from space: The Sentinel-2 multispectral capabilities. *Rem. Sens. Env.*, 234:111468, 2019. doi:10.1016/j.rse.2019.111468.

- B.K. Arbic, A.J. Wallcraft, and E.J. Metzger. Concurrent simulation of the eddying general circulation and tides in a global ocean model. *Ocean Modelling*, 32(3):175–187, 2010. doi:10.1016/j.ocemod.2010.01.007.
- Yongsheng Xu and Lee-Lueng Fu. The Effects of Altimeter Instrument Noise on the Estimation of the Wavenumber Spectrum of Sea Surface Height. *Journal of Physical Oceanography*, 42(12):2229–2233, August 2012. ISSN 0022-3670. doi:10.1175/JPO-D-12-0106.1.
- C. Shorten and T.M. Chin. A survey on Image Data Augmentation for Deep Learning. *Journal of Big Data*, 6(1):60, July 2019. ISSN 2196-1115. doi:10.1186/s40537-019-0197-0.
- H. Wang, N. Grisouard, H. Salehipour, A. Nuz, M. Poon, and A.L. Ponte. A Deep Learning Approach to Extract Internal Tides Scattered by Geostrophic Turbulence. *Geophysical Res. Lett.*, 49(11):e2022GL099400, 2022. doi:10.1029/2022GL099400.
- E. Martinez, A. Brini, T. Gorgues, L. Drumetz, J. Roussillon, P. Tandeo, G. Maze, and R. Fablet. Neural Network Approaches to Reconstruct Phytoplankton Time-Series in the Global Ocean. *Rem. Sens.*, 12(24):4156, 2020. doi:10.3390/rs12244156.
- S.A. Boukabara, K. Ide, Y. Zhou, N. Shahroudi, R.N. Hoffman, K. Garrett, V.K. Kumar, T. Zhu, and R. Atlas. Community Global Observing System Simulation Experiment (OSSE) Package (CGOP): Assessment and Validation of the OSSE System Using an OSSE–OSE Intercomparison of Summary Assessment Metrics. *J. Atm. Ocean. Tech.*, 35(10):2061–2078, 2018. doi:10.1175/JTECH-D-18-0061.1.
- J.M. Vient, F. Jourdin, R. Fablet, B. Mengual, L. Lafosse, and C. Delacourt. Data-Driven Interpolation of Sea Surface Suspended Concentrations Derived from Ocean Colour Remote Sensing Data. *Rem. Sens.*, 13(17):3537, 2021. doi:10.3390/rs13173537.
- A. Puissant, R. El Hourany, A.A. Charantonis, C. Bowler, and S. Thiria. Inversion of Phytoplankton Pigment Vertical Profiles from Satellite Data Using Machine Learning. *Rem. Sens.*, 13(8):1445, 2021. ISSN 2072-4292. doi:10.3390/rs13081445.
- G. Cossarini, L. Mariotti, L. Feudale, A. Mignot, S. Salon, V. Taillandier, A. Teruzzi, and F. D’Ortenzio. Towards operational 3D-Var assimilation of chlorophyll Biogeochemical-Argo float data into a biogeochemical model of the Mediterranean Sea. *Ocean Mod.*, 133:112–128, January 2019. doi:10.1016/j.ocemod.2018.11.005.
- D. Roemmich, M.H. Alford, H. Claustre, Kenneth Johnson, Brian King, James Moum, Peter Oke, W. Brechner Owens, Sylvie Pouliquen, Sarah Purkey, Megan Scanderbeg, Toshio Suga, Susan Wijffels, Nathalie Zilberman, Dorothee Bakker, Molly Baringer, Mathieu Belbeoch, Henry C. Bittig, Emmanuel Boss, Paulo Calil, Fiona Carse, Thierry Carval, Fei Chai, Diarmuid Ó. Conchubhair, Fabrizio d’Ortenzio, Giorgio Dall’Olmo, Damien Desbruyeres, Katja Fennel, Ilker Fer, Raffaele Ferrari, Gael Forget, Howard Freeland, Tetsuichi Fujiki, Marion Gehlen, Blair Greenan, Robert Hallberg, Toshiyuki Hibiya, Shigeki Hosoda, Steven Jayne, Markus Jochum, Gregory C. Johnson, KiRyong Kang, Nicolas Kolodziejczyk, Arne Körtzinger, Pierre-Yves Le Traon, Yueng-Djern Lenn, Guillaume Maze, Kjell Arne Mork, Tamaryn Morris, Takeyoshi Nagai, Jonathan Nash, Alberto Naveira Garabato, Are Olsen, Rama Rao Pattabhi, Satya Prakash, Stephen Riser, Catherine Schmechtig, Claudia Schmid, Emily Shroyer, Andreas Sterl, Philip Sutton, Lynne Talley, Toste Tanhua, Virginie Thierry, Sandy Thomalla, John Toole, Ariel Troisi, Thomas W. Trull, Jon Turton, Pedro Joaquin Velez-Belchi, Waldemar Walczowski, Haili Wang, Rik Wanninkhof, Amy F. Waterhouse, Stephanie Waterman, Andrew Watson, Cara Wilson, Annie P. S. Wong, Jianping Xu, and I. Yasuda. On the Future of Argo: A Global, Full-Depth, Multi-Disciplinary Array. *Front. Mar. Sc.*, 6, 2019. ISSN 2296-7745. doi:10.3389/fmars.2019.00439.
- A. Storto, S. Falchetti, P. Oddo, Y.M. Jiang, and A. Tesei. Assessing the Impact of Different Ocean Analysis Schemes on Oceanic and Underwater Acoustic Predictions. *J. Geophys. Res.*, 125(7):e2019JC015636, 2020. doi:10.1029/2019JC015636.
- A. Storto, G.D. Magistris, S. Falchetti, and P. Oddo. A Neural Network–Based Observation Operator for Coupled Ocean–Acoustic Variational Data Assimilation. *Month. Weath. Rev.*, 149(6):1967–1985, 2021. doi:10.1175/MWR-D-20-0320.1.

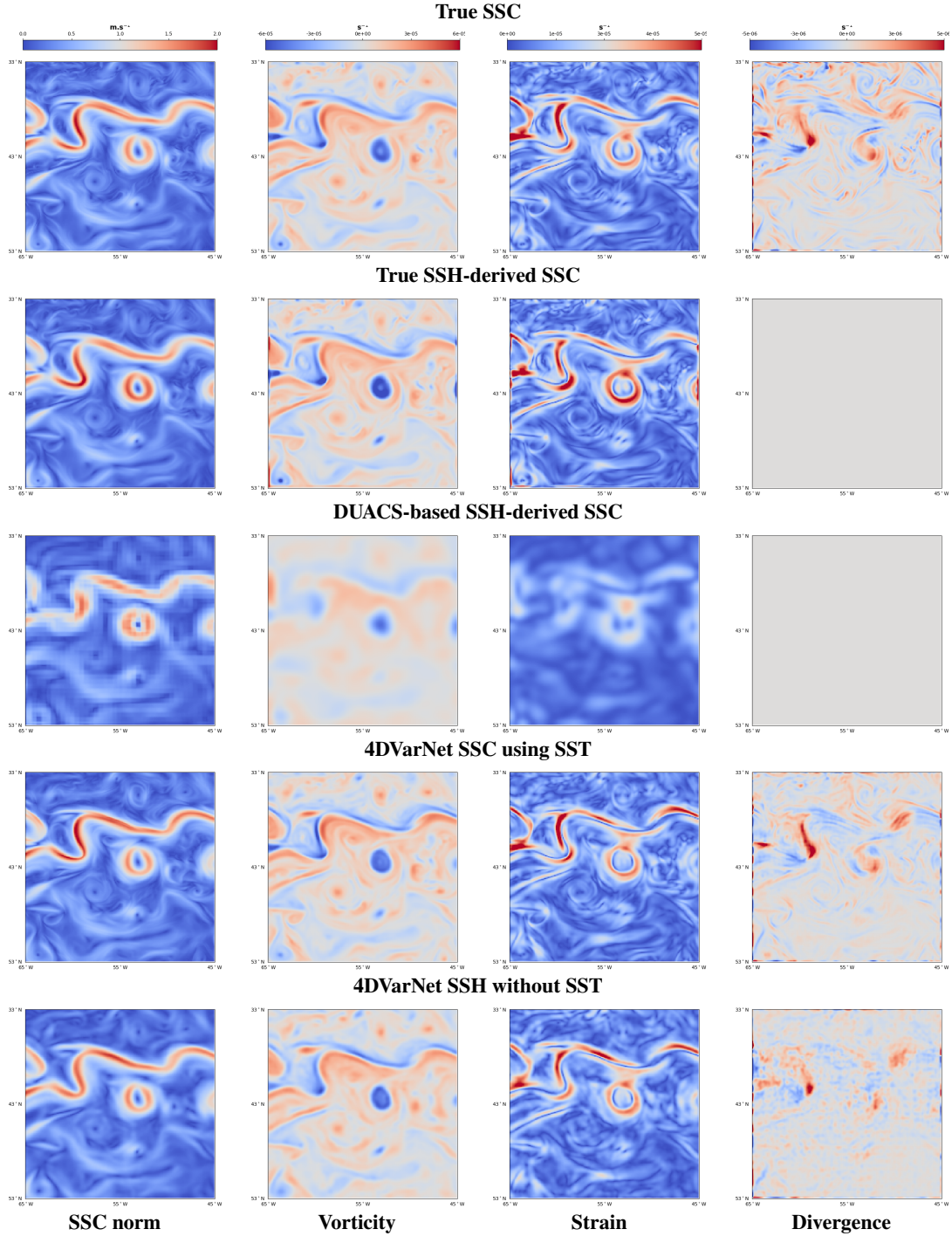


Figure 3: **Reconstructed SSC fields on November 12th 2012:** From left to right, we depict the norm (i.e., velocity intensity), the vorticity, the divergence and the strain of SSC fields corresponding respectively to, from top to bottom, the true SSC field, the SSH-derived one, DUACS-derived one, and 4DVarNet-derived using SSH-SST fields and using only-SSH field.

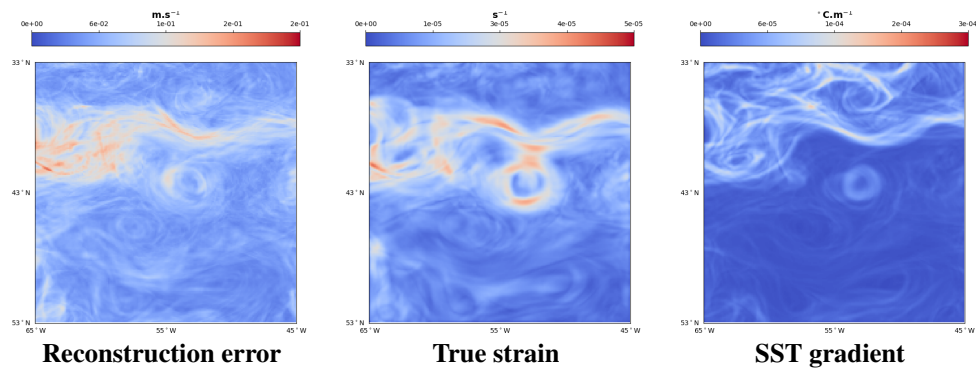


Figure 4: **Time-averaged reconstruction error vs. mean strain field and SST gradient over the whole test dataset:** from left to right, we display the time-averaged mean square reconstruction error field of the SSC using the 4DVarNet scheme combining altimetry and SST observations, the time-averaged true strain field and the time-averaged SST gradient. The coefficient of determination between the error field and the later fields is respectively of 59% and 24%. The reconstructed strain field depicted in Fig.3 leads to an explained variance of 57% for the time-averaged reconstruction error.